AIAA JOURNAL
Vol. 48, No. 6, June 2010

Validation of Fully Implicit, Parallel Finite Element Simulations of Laminar Hypersonic Flows

Benjamin S. Kirk*
NASA Lyndon B. Johnson Space Center, Houston, Texas 77058
and
Graham F. Carey†
University of Texas at Austin, Austin, Texas 78712

DOI: 10.2514/1.40860

This paper concerns comparative studies of predictive simulations and experimental results from the literature for high-Mach-number two-dimensional/axisymmetric flow past a hollow-cylinder flare and a double cone. The underlying physical model for the mathematical formulation assumes calorically-perfect-gas laminar flow, and we seek to approximate the corresponding compressible Navier–Stokes equations expressed in conservation-variable form. Predictive simulations of this mathematical model are based on a fully implicit, parallel streamline-upwind Petrov–Galerkin finite element formulation that uses a grouped-variable expansion for the inviscid flux terms. The spatial discretization, second-order-accurate time discretization, numerical method, and parallel fully implicit implementation are concisely described. Representative iterative and mesh convergence results are presented for the case of a hollow-cylinder flare. Local predicted values of surface pressure and heat transfer are compared with available experimentally measured values for both geometries. These results are interpreted in the context of validation. Predicted results for complex flowfield/shock interactions and the viscous slip surface are illustrated through a computed schlieren image for the double cone. The present work presents the first known comparison of predictions from the finite element method to this set of data, and the validation study provides the comparative details to motivate future computational investigations and experimental studies.

Nomenclature

$\boldsymbol{A}_i$ = inviscid flux Jacobian, $\partial \boldsymbol{F}_i / \partial \boldsymbol{U}$
$\boldsymbol{A}_0^{-1}$ = mapping from conservation to entropy variables
c_p = specific heat at constant pressure
c_v = specific heat at constant volume
E = total energy per unit mass, $e + \frac{1}{2}\boldsymbol{u} \cdot \boldsymbol{u}$
e = internal energy per unit mass, $c_v T$
$\boldsymbol{F}_i$ = inviscid flux vector (e.g., $[\rho u, \rho u^2 + P, \rho u v, \rho u H]^T$)
$\boldsymbol{G}_i$ = viscous flux vector
H = total enthalpy, $E + P/\rho$
h = element reference length
$\boldsymbol{K}_{ij}$ = diffusivity matrix
k = thermal conductivity
$\hat{\boldsymbol{n}}$ = surface unit normal vector
P = pressure
Pr = Prandtl number, $\mu c_p / k$
$\boldsymbol{q}$ = heat flux vector, $-k \nabla T$
R = ideal-gas constant
$\boldsymbol{R}$ = nonlinear residual
$\mathcal{R}$ = discrete unsteady residual
r = time-step growth rate
T = temperature
t = time
$\boldsymbol{U}$ = vector of conservation variables, $[\rho, \rho u, \rho v, \rho E]^T$
$\boldsymbol{u}$ = velocity
$\boldsymbol{W}$ = finite element test function
$\alpha_t, \beta_t, \gamma_t$ = time-discretization coefficients
Δt = time step
δ = shock-capturing function
Γ = computational domain boundary
γ = ratio of specific heats, c_p / c_v
ξ, η, ζ = reference element coordinates
μ = dynamic viscosity
ρ = density
$\{\phi\}$ = set of finite element shape functions
$\boldsymbol{\tau}$ = viscous stress tensor
$\boldsymbol{\tau}_{\mathrm{SUPG}}$ = streamline–upwind Petrov–Galerkin stabilization matrix of intrinsic time scales
Ω = computational domain

Subscript

i = dimension index, $\in (1, \mathrm{DIM})$

I. Introduction

THE reliability of predictive simulations and the formulation of more rigorous approaches for verification of numerical schemes and validation of approximate models is a topic of increasing interest and importance [1–3]. A formal framework and rigorous testing for verification and validation of complex predictive simulations is an extensive and formidable undertaking. One key component in the validation component of this framework is comparison of predictive results for a well-founded model against available benchmark experimental results. Typically, such experimental measured values are sparse and their reliability is also an issue in this context. The focus of the present work is the comparative evaluation for predictive simulation of a class of high-speed compressible flows. Two well-documented high-quality experimental data sets are chosen for the basis of this comparison [4–9].

Compressible flows encompass a wide range of applications that of are of particular interest in the design and analysis of atmospheric flight and entry vehicles. The complexity of the phenomenological behavior and associated models is quite diverse, including laminar, transitional, and turbulent flow and gases that may be out of thermal

---

Received 7 September 2008; revision received 13 November 2009; accepted for publication 19 January 2010. This material is declared a work of the U.S. Government and is not subject to copyright protection in the United States. Copies of this paper may be made for personal or internal use, on condition that the copier pay the $10.00 per-copy fee to the Copyright Clearance Center, Inc., 222 Rosewood Drive, Danvers, MA 01923; include the code 0001-1452/10 and $10.00 in correspondence with the CCC.

*Aerospace Engineer, Applied Aeroscience and Computational Fluid Dynamics Branch, 2101 NASA Parkway, Mail Code EG3. Member AIAA.

†Professor, Institute for Computational Engineering Sciences, Mail Code C0600.

and chemical equilibrium. Hence, some care must be exercised in delineating the flow class for the comparative evaluation against experiment and in interpretation of the ensuing results of the comparison. In the present work, the benchmark experimental results are for high-speed axisymmetric flow past a hollow-cylinder flare and a double cone with both blunt and sharp nose tips [4,6,7]. The respective hollow-cylinder-flare and blunt-double-cone cases were tested experimentally by Holden and Wadhams [4] and Wadhams and Holden [5]. Both examples feature separated flowfields and shock/boundary-layer interaction, which are fundamental processes that are characteristic of the application class, making them particularly well-suited for the goals of this study. Additionally, since both cases are two-dimensional, rigorous mesh refinement studies can be performed with only moderate cost.

The flow conditions and previous experimental studies of these two cases suggest that a viable physical model for comparative simulations may be based on laminar flow of a calorically perfect gas, and this is a flow class of broad practical interest for atmospheric flight and entry vehicles. This flow class is modeled mathematically by the corresponding conservation form of the compressible Navier–Stokes equations. A weak variational formulation and finite element approximation scheme is constructed for predictive simulations. The discrete approximation is implemented on top of the libMesh parallel adaptive finite element library [10] with a fully implicit algorithm. The time-discretization and nonlinear solution aspects used in the computational algorithm are summarized later.

The basic finite element method and algorithm have been verified in a previous study for classical problems and problems with manufactured solutions [11,12]. Our purpose here is to conduct a validation step via comparison to experimental measurements for the two demanding test cases introduced earlier. Interpretation of the comparison will help assess the validity of the modeling assumptions, and it will also provide a more stringent test of the methodology and algorithm than the simpler verification studies.

The remainder of this paper is outlined as follows. For specificity, Sec. II summarizes the chosen mathematical model for compressible flow of a laminar calorically perfect gas and associated transport properties. Section III then presents the stabilized weak form of the governing equations, and Sec. IV describes the associated finite element discretization. The parallel solution methodology and algorithms are described in Sec. V. The results of the simulations are presented in Sec. VI, and the quantities of interest for the comparison study (measured surface pressure and heat transfer coefficients) are graphed and interpreted. The important question of iterative and mesh convergence are addressed for the case of a hollow-cylinder flare. Finally, some general observations arising from the study are summarized and open issues are discussed in Sec. VII.

II. Mathematical Model

The compressible Navier–Stokes equations describe the conservation of mass, momentum, and energy for this class of flows. The conservation of mass, momentum, and energy for a compressible fluid may be written as

$$\frac{\partial \rho}{\partial t} + \nabla \cdot (\rho \boldsymbol{u}) = 0 \tag{1}$$

$$\frac{\partial \rho \boldsymbol{u}}{\partial t} + \nabla \cdot (\rho \boldsymbol{u}\boldsymbol{u}) = -\nabla P + \nabla \cdot \boldsymbol{\tau} \tag{2}$$

$$\frac{\partial \rho E}{\partial t} + \nabla \cdot (\rho E \boldsymbol{u}) = -\nabla \cdot \boldsymbol{q} - \nabla \cdot (P\boldsymbol{u}) + \nabla \cdot (\boldsymbol{\tau}\boldsymbol{u}) \tag{3}$$

where $\boldsymbol{\tau} = \mu(\nabla \boldsymbol{u} + \nabla^T \boldsymbol{u}) - \frac{2}{3}\mu(\nabla \cdot \boldsymbol{u})\boldsymbol{I}$. In three dimensions, Eqs. (1–3) provide a system of five coupled partial differential equations in the seven unknowns ρ, $\boldsymbol{u}$, e, P, and T, provided that the transport properties μ and k may be related to the unknown thermodynamic properties. Clearly, two additional equations are required to close the system. These additional equations are equations of state that relate the thermodynamic variables ρ, e, P, and T. Assuming that the fluid is in thermodynamic equilibrium, its state is fixed by any two independent thermodynamic variables. Thus, by choosing ρ and e to be the independent variables, state equations for $P = P(\rho, e) = (\gamma - 1)\rho e$ and $T = T(e) = (\gamma - 1)e/R$ may be obtained. These state equations are valid for a calorically perfect gas, which is appropriate for nitrogen (the test gas considered in subsequent experimental comparisons) at stagnation temperatures below roughly 3500 K.

The remaining coefficients of viscosity and thermal conductivity may be related to the thermodynamic variables using kinetic theory [13]. For nitrogen over a wide range of temperatures, $\mu = \mu(T)$ and is given by Sutherland's law [14]:

$$\mu = 1.399 \times 10^{-6} \frac{T^{\frac{3}{2}}}{T + 106.67} \tag{4}$$

where T is measured in Kelvin, and μ is given in pascal seconds. With the viscosity given by Eq. (4) for a given temperature, it is convenient to determine the thermal conductivity k assuming a constant Prandtl number $Pr = 0.71$. This modeling assumption is justified for this hypersonic flow because of the relatively low static temperatures in the shock layer.

Equations (1–3) may be written in conservative system form as

$$\frac{\partial \boldsymbol{U}}{\partial t} + \frac{\partial \boldsymbol{F}_i}{\partial x_i} = \frac{\partial \boldsymbol{G}_i}{\partial x_i} \tag{5}$$

The second term on the left-hand side of Eq. (5) is the divergence of the inviscid flux vector $\partial \boldsymbol{F}_i/\partial x_i$ and may be written in terms of the unknowns $\boldsymbol{U}$ as

$$\frac{\partial \boldsymbol{F}_i}{\partial x_i} = \frac{\partial \boldsymbol{F}_i}{\partial \boldsymbol{U}} \frac{\partial \boldsymbol{U}}{\partial x_i} = \boldsymbol{A}_i \frac{\partial \boldsymbol{U}}{\partial x_i} \tag{6}$$

Similarly, the viscous flux vector $\boldsymbol{G}_i$ may be written as

$$\frac{\partial \boldsymbol{G}_i}{\partial x_i} = \frac{\partial}{\partial x_i}\left(\boldsymbol{K}_{ij} \frac{\partial \boldsymbol{U}}{\partial x_j}\right) \tag{7}$$

The matrices $\boldsymbol{A}_i$ and $\boldsymbol{K}_{ij}$ $[\partial \boldsymbol{G}_i/\partial x_i = \partial/\partial x_i(\boldsymbol{K}_{ij}(\partial \boldsymbol{U}/\partial x_j))]$ are both functions of the independent variables $\boldsymbol{U}$ and are listed explicitly in [11]. Using Eq. (7) in Eq. (5) yields the second-order system

$$\frac{\partial \boldsymbol{U}}{\partial t} + \frac{\partial \boldsymbol{F}_i}{\partial x_i} = \frac{\partial}{\partial x_i}\left(\boldsymbol{K}_{ij} \frac{\partial \boldsymbol{U}}{\partial x_j}\right) \tag{8}$$

which will be the basis for developing a weak formulation in Sec. III.

III. Weak Formulation

The corresponding weak form of the governing system of equations (8) may be constructed in the standard way by first multiplying by an appropriate set of test functions $\boldsymbol{W}$ and integrating over the domain Ω. Integrating the viscous term by parts yields the weak statement: Find $\boldsymbol{U}$ satisfying the essential boundary and initial conditions such that

$$\int_\Omega \left[\boldsymbol{W} \cdot \left(\frac{\partial \boldsymbol{U}}{\partial t} + \frac{\partial \boldsymbol{F}_i}{\partial x_i}\right) + \frac{\partial \boldsymbol{W}}{\partial x_i} \cdot \left(\boldsymbol{K}_{ij} \frac{\partial \boldsymbol{U}}{\partial x_j}\right)\right] \mathrm{d}\Omega - \oint_\Gamma \boldsymbol{W} \cdot \boldsymbol{g} \, \mathrm{d}\Gamma = 0 \tag{9}$$

for all $\boldsymbol{W}$ in an appropriate function space. In the last term, $\boldsymbol{g} = \boldsymbol{G} \cdot \hat{\boldsymbol{n}}$ is the normal component of the viscous flux on the boundary Γ with unit normal $\hat{\boldsymbol{n}}$.

A standard Galerkin finite element formulation as presented in Eq. (9) (or similar finite difference or finite volume strategies) is unstable in the sense that it may produce nonphysical oscillations in regions of steep solution gradients or strong convection. Even when viscous effects are included as in Eq. (9), standard Galerkin calculations may produce nonphysical oscillations for convection-dominated flows. This well-known phenomenon results because the standard Galerkin formulation (or, equivalently, central differencing on a structured grid) produces a difference stencil whose solution admits oscillatory behavior [15–17].

Several techniques have been proposed to address the stability issue of the Galerkin formulation. The familiar Lax–Wendroff finite difference scheme produces the Taylor–Galerkin scheme in the context of finite elements. The Taylor–Galerkin scheme employs a second-order Taylor series in time and an interchange of spatial and temporal differentiation in the discretization of Eq. (5). This yields a second-order term in the discrete form that can be interpreted as a stabilizing diffusion. Recently, the Taylor–Galerkin scheme has been applied to hypersonic flowfields in chemical and thermal nonequilibrium [18] and high-order Navier–Stokes discretizations [19], illustrating its applicability to the class of problems considered in the present work.

A different approach is pursued [20,21] in the least-squares finite element method. In the least-squares approach, the test function $\boldsymbol{W}$ in Eq. (9) is replaced by the variation of the residual of the governing equations. Conceptually, this is equivalent to minimizing the residual in a least–squares sense. A detailed analysis of this formulation reveals a stabilizing mechanism similar to the Taylor–Galerkin scheme. This least–squares idea can be combined with the Galerkin statement to yield the so-called Galerkin/least–squares scheme [22].

The stabilization introduced via numerical dissipation in upwind differencing can be achieved in the finite element setting when an upwind bias is added to the test function $\boldsymbol{W}$. This idea, and the need to reduce crosswind dissipation in two or three dimensions, led to the development of the directed streamline-upwind Petrov–Galerkin (SUPG) formulation as another stabilizing mechanism for convection-dominated flows [23]. For the system of equations (8), a suitably upstream-biased test function can be defined by augmenting the standard Galerkin test function $\boldsymbol{W}$ with the convective operator acting on the test function:

$$\hat{\boldsymbol{W}} = \boldsymbol{W} + \boldsymbol{\tau}_{\mathrm{SUPG}} \boldsymbol{A}_i \frac{\partial \boldsymbol{W}}{\partial x_i} \tag{10}$$

The stabilization matrix $\boldsymbol{\tau}_{\mathrm{SUPG}}$ plays an important role in the SUPG formulation in that it seeks to introduce the minimal amount of diffusion necessary to stabilize the scheme. In this work, $\boldsymbol{\tau}_{\mathrm{SUPG}}$ is adapted from previous work by Shakib et al. [24] in the context of entropy variables and later used with the conservation variables [25,26]. Specifically, in three dimensions,

$$\boldsymbol{\tau}_{\mathrm{SUPG}} = \mathrm{diag}(\tau_c, \tau_m, \tau_m, \tau_m, \tau_e) \tag{11}$$

where τ_c, τ_m, and τ_e are scalar stabilization parameters for the continuity, momentum, and energy equations, respectively, and are given by

$$\tau_c = \left[\left(\frac{2}{\Delta t}\right)^2 + \left(\frac{2(\|\boldsymbol{u}\| + c)}{h_{\boldsymbol{u}}}\right)^2\right]^{-1/2}$$

$$\tau_m = \left[\left(\frac{2}{\Delta t}\right)^2 + \left(\frac{2(\|\boldsymbol{u}\| + c)}{h_{\boldsymbol{u}}}\right)^2 + \left(\frac{4\mu}{\rho h_{\boldsymbol{u}}^2}\right)^2\right]^{-1/2}$$

$$\tau_e = \left[\left(\frac{2}{\Delta t}\right)^2 + \left(\frac{2(\|\boldsymbol{u}\| + c)}{h_{\boldsymbol{u}}}\right)^2 + \left(\frac{4k}{\rho c_p h_{\boldsymbol{u}}^2}\right)^2\right]^{-1/2}$$

and are designed to transition smoothly between convective-, diffusive-, and transitive-dominated flow regimes. The diagonal form of the stabilization matrix $\boldsymbol{\tau}_{\mathrm{SUPG}}$ is commonly applied in convection-dominated compressible flows [27]. The flow-aligned element length scale $h_{\boldsymbol{u}}$ is defined as

$$h_{\boldsymbol{u}} = 2\left(\sum_{k=1}^{\text{no. nodes}} |\hat{\boldsymbol{u}} \cdot \nabla\phi_k|\right)^{-1} \tag{12}$$

where the shape functions in Eq. (12) are the typical *unbiased* finite element shape functions. Here, it has been assumed that a standard Lagrange basis is used, and the sum extends over the number of shape functions (which is equal to the number of nodes in the element).

It is important to note that all of the schemes discussed previously only address instabilities induced by strong convection. For supersonic problems involving strong shock waves, another form of stabilization is required. More specifically, a local regularization scheme using a shock-capturing function is required to eliminate nonphysical over- and undershoots induced by strong gradients. The regularized SUPG weak statement then follows by multiplying Eq. (8) by Eq. (10) and integrating by parts as before:

$$\begin{aligned}
&\int_\Omega \left[\boldsymbol{W} \cdot \left(\frac{\partial \boldsymbol{U}}{\partial t} + \frac{\partial \boldsymbol{F}_i}{\partial x_i}\right) + \frac{\partial \boldsymbol{W}}{\partial x_i} \cdot \left(\boldsymbol{K}_{ij} \frac{\partial \boldsymbol{U}}{\partial xj}\right)\right] \mathrm{d}\Omega \\
&\quad + \sum_{e=1}^{n_{\mathrm{el}}} \int_{\Omega_e} \boldsymbol{\tau}_{\mathrm{SUPG}} \frac{\partial \boldsymbol{W}}{\partial x_k} \cdot \boldsymbol{A}_k \left[\frac{\partial \boldsymbol{U}}{\partial t} + \frac{\partial \boldsymbol{F}_i}{\partial x_i} - \frac{\partial}{\partial x_i}\left(\boldsymbol{K}_{ij} \frac{\partial \boldsymbol{U}}{\partial xj}\right)\right] \mathrm{d}\Omega \\
&\quad + \sum_{e=1}^{n_{el}} \int_{\Omega_e} \delta\left(\frac{\partial \boldsymbol{W}}{\partial x_i} \cdot \frac{\partial \boldsymbol{U}}{\partial x_i}\right) \mathrm{d}\Omega - \oint_\Gamma \boldsymbol{W} \cdot \boldsymbol{g}\, \mathrm{d}\Gamma = 0
\end{aligned} \tag{13}$$

The shock-capturing function is local and essentially regularizes the problem by selectively introducing isotropic artificial diffusion. This added local dissipation captures shocks across approximately a few mesh cells.

The shock-capturing function was adapted for a system of conservation variables [25,26,28] from the original definition employed for the case of entropy variables [24,29] and is given by

$$\delta = \left[\frac{\| \frac{\partial \boldsymbol{U}}{\partial t} + \frac{\partial \boldsymbol{F}_i}{\partial x_i} - \frac{\partial}{\partial x_i}(\boldsymbol{K}_{ij} \frac{\partial \boldsymbol{U}}{\partial xj}) \|^2_{\boldsymbol{A}_0^{-1}}}{\|\nabla\xi \cdot \nabla\boldsymbol{U}\|^2_{\boldsymbol{A}_0^{-1}} + \|\nabla\eta \cdot \nabla\boldsymbol{U}\|^2_{\boldsymbol{A}_0^{-1}} + \|\nabla\zeta \cdot \nabla\boldsymbol{U}\|^2_{\boldsymbol{A}_0^{-1}}}\right]^{1/2} \tag{14}$$

The physical-domain- to-reference-domain element transformation terms $\nabla\xi$, $\nabla\eta$, and $\nabla\zeta$ are $\mathcal{O}(1/h)$; hence, δ is proportional to h. Thus, in regions of appreciable δ, Eq. (13) reduces to an $\mathcal{O}(h)$ approximation of Eq. (5) for a piecewise-linear finite element approximation.

Note that the combination of streamline-upwinding and shock-capturing required to obtain stable solutions with the finite element method is similar to the upwinding and limiting that is characteristic of total-variation-diminishing (TVD) finite difference and finite volume schemes. TVD schemes typically employ an upwind treatment of the inviscid flux terms that is sufficient to stabilize convection-dominated flows. However, flux or slope limiters, which are designed to restore monotonicity, are required in the presence of strong shock waves. The shock-capturing function used in the present scheme is similar to the use of limiters in that it attempts to restore monotonicity in regions of large gradients such as shock waves. (In general, monotonicity can only be guaranteed for the one-dimensional case.) Both TVD finite volume schemes and the current finite element schemes reduce to first order at shock waves in an attempt to restore monotonicity of the solution.

Hypersonic viscous flows are considered in the subsequent numerical studies. For this class of flows the Navier–Stokes equations form a mixed parabolic–hyperbolic set of partial differential equations. Three classes of boundary conditions relevant to the problem class of interest follow:

1) At supersonic inflow boundaries, the characteristics of the system are all directed into the domain; hence, each component of the system may be specified as an essential boundary condition. In general, for aerothermodynamic applications, the freestream density, velocity, and temperature are usually prescribed. With these primitive variables specified, the conservation variables may be determined using a suitable state equation.

2) At the surface of a body in a viscous flow, the no-slip isothermal boundary condition in which $T = T_w$ is applied. The no-slip condition is implemented simply by specifying appropriate essential boundary conditions for the momentum components of the equation system. The isothermal boundary condition is implemented as an essential condition on the total energy per unit volume, ρE. At a no-slip wall we have

$$\rho E = \rho\left(e + \frac{\boldsymbol{u} \cdot \boldsymbol{u}}{2}\right) = \rho e = \rho c_v T_w$$

which is implemented as the essential implicit boundary condition $\rho E - \rho c_v T_w = 0$.

3) At supersonic outflow boundaries the state is defined entirely by the internal conditions. However, as pointed out by Hauke and Hughes [30], it is important to include the viscous boundary terms that result from the integration by parts performed in Eq. (13). These boundary-term contributions are computed at viscous supersonic outflow boundaries and are included in the system matrix.

IV. Finite Element Formulation

Upon introducing a finite element discretization and corresponding basis to define the approximate solution $\boldsymbol{U}_h$ and test functions $\boldsymbol{W}_h$, and substituting into Eq. (13), the corresponding approximate finite element formulation has the following form: Find $\boldsymbol{U}_h$ satisfying the essential boundary and initial conditions such that

$$\begin{aligned}&\int_\Omega \left[\boldsymbol{W}_h \cdot \left(\frac{\partial \boldsymbol{U}_h}{\partial t} + \frac{\partial \boldsymbol{F}_{i,h}}{\partial x_i}\right) + \frac{\partial \boldsymbol{W}_h}{\partial x_i} \cdot \left(\boldsymbol{K}_{ij} \frac{\partial \boldsymbol{U}_h}{\partial xj}\right)\right] \mathrm{d}\Omega \\ &\quad + \sum_{e=1}^{n_{\mathrm{el}}} \int_{\Omega_e} \boldsymbol{\tau}_{\mathrm{SUPG}} \frac{\partial \boldsymbol{W}_h}{\partial x_k} \cdot \boldsymbol{A}_k \left[\frac{\partial \boldsymbol{U}_h}{\partial t} + \frac{\partial \boldsymbol{F}_{i,h}}{\partial x_i} - \frac{\partial}{\partial x_i}\left(\boldsymbol{K}_{ij} \frac{\partial \boldsymbol{U}_h}{\partial x_j}\right)\right] \mathrm{d}\Omega \\ &\quad + \sum_{e=1}^{n_{\mathrm{el}}} \int_{\Omega_e} \delta \left(\frac{\partial \boldsymbol{W}_h}{\partial x_i} \cdot \frac{\partial \boldsymbol{U}_h}{\partial x_i}\right) \mathrm{d}\Omega - \oint_\Gamma \boldsymbol{W}_h \cdot \boldsymbol{g}_h \, \mathrm{d}\Gamma = 0 \end{aligned} \tag{15}$$

for all admissible test functions $\boldsymbol{W}_h$.

More specifically, let us expand $\boldsymbol{U}_h(\boldsymbol{x}, t)$ and $\boldsymbol{F}_{i,h}(\boldsymbol{x}, t)$ in terms of the finite element basis functions:

$$\boldsymbol{U}_h(\boldsymbol{x}, t) = \sum_j \phi_j(\boldsymbol{x}) \boldsymbol{U}_h(\boldsymbol{x}_j, t) \tag{16}$$

$$\boldsymbol{F}_{i,h}(\boldsymbol{x}, t) = \sum_j \phi_j(\boldsymbol{x}) \boldsymbol{F}_{i,h}(\boldsymbol{x}_j, t) = \sum_j \phi_j(\boldsymbol{x}) \boldsymbol{A}_i(\boldsymbol{U}_h(\boldsymbol{x}_j, t)) \boldsymbol{U}_h(\boldsymbol{x}_j, t) \tag{17}$$

where $\boldsymbol{U}_h(\boldsymbol{x}_j, t)$ and $\boldsymbol{F}_{i,h}(\boldsymbol{x}_j, t)$ are the nodal solution values and nodal inviscid flux components at time t, respectively. The grouped-variable discretization of $\boldsymbol{F}_{i,h}$ is nonstandard, but has shown to improve some aspects of the numerical scheme [12]. In this work, a standard piecewise-linear Lagrange basis is chosen for $\{\phi\}$, which yields a nominally-second-order-accurate scheme. Since the focus here is on supersonic flows that exhibit shock waves, no attempt has been made to achieve higher–order spatial discretizations. However, previous work with a similar formulation for the compressible Navier–Stokes equations suggests that the current scheme could easily be extended to higher order for flows without shocks simply by using a higher-order finite element basis [31].

V. Solution Methodology

Equation (15) forms a transient tightly coupled nonlinear system for the unknown nodal values $\boldsymbol{U}_h(\boldsymbol{x}_j, t)$. Even when a steady solution to the governing equations is sought, Eqs. (15) are often solved with a pseudo-time-continuation strategy. That is, even for steady problems, the unsteady equations are often integrated in time until steady state is reached. This is especially the case for compressible flows containing shock waves, because strong gradients that occur in the flow imply an extremely small zone of attraction for nonlinear implicit solution schemes such as Newton's method [32,33]. Algorithms for solving this type of transient system fall broadly into two categories: explicit and implicit.

Since the present work seeks to ultimately use adaptive meshing techniques to locally resolve fine features of the flow (thus decreasing the element size h), the h dependence of Δt for explicit schemes is particularly unattractive [34]. The cost for seeking this increased stability is the need to solve (at least approximately) a nonlinear implicit system at each time step of the solution. Preconditioned Krylov subspace iterative methods provide a suitable choice of solvers that are amenable to parallel solution and are efficient for the problems of interest here [35].

The remainder of this section describes 1) the domain-decomposition approach used to achieve parallelism, 2) the time integration scheme, and 3) linearization strategies used for both steady-state and time-accurate flows. The iterative techniques used to solve the resulting linear systems will also be briefly discussed.

A standard nonoverlapping domain-decomposition scheme is used in which a unique set of elements is assigned to each processor used in the simulation (see [10] and references therein). The METIS unstructured graph partitioning library [36] is used to create a weighted partition that attempts to balance the computational load incurred for a hybrid element unstructured mesh. An example decomposition into six subdomains is shown in Fig. 1 for the case of an axisymmetric cylinder flare. Each subdomain contains approximately the same number of elements.

The domain-decomposition approach allows element contributions to the global implicit system to be calculated in parallel. That is, each processor will form the system matrix contributions only for its local elements. These contributions are then accumulated into a distributed sparse matrix data structure, which is ultimately used in an iterative Krylov subspace technique to both precondition and approximately solve the linear system [10,11,37].

As mentioned previously, steady solutions are often found by time-marching the transient governing equations to steady state. In this sense, the initial condition is taken at time $t = 0$ and the solution is marched in time until $\partial \boldsymbol{U}/\partial t \to 0$. In this way, time is essentially a continuation parameter that defines a sequence ($n = 1, 2, \ldots$) of solutions $\boldsymbol{U}_n$ that converge to the steady solution $\boldsymbol{U}$.

The semidiscrete weak form in Eq. (15) is discretized about time $t = t_{n+1}$ using backward finite difference schemes. Both first- and second-order-accurate-in-time schemes may be derived from Taylor series expansions in time about $\boldsymbol{U}_h(t_{n+1}) = \boldsymbol{U}_{n+1}$,

$$\begin{aligned}\boldsymbol{U}_n &= \boldsymbol{U}_{n+1} + \frac{\partial \boldsymbol{U}_{n+1}}{\partial t}(t_n - t_{n+1}) + \frac{\partial^2 \boldsymbol{U}_{n+1}}{\partial t^2}\frac{(t_n - t_{n+1})^2}{2} \\ &\quad + \mathcal{O}((t_n - t_{n+1})^3) \\ \boldsymbol{U}_{n-1} &= \boldsymbol{U}_{n+1} + \frac{\partial \boldsymbol{U}_{n+1}}{\partial t}(t_{n-1} - t_{n+1}) + \frac{\partial^2 \boldsymbol{U}_{n+1}}{\partial t^2}\frac{(t_{n-1} - t_{n+1})^2}{2} \\ &\quad + \mathcal{O}((t_{n-1} - t_{n+1})^3)\end{aligned}$$

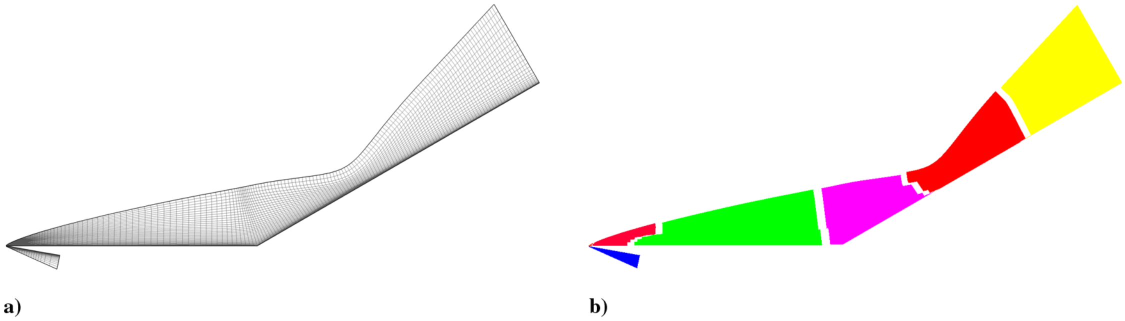

Fig. 1 Illustrations of a) computational mesh (every other point shown) and b) resulting parallel domain decomposition for an axisymmetric hollow-cylinder flare.

which, upon substituting $t_{n+1} - t_n \equiv \Delta t_{n+1}$ and $t_{n+1} - t_{n-1} = \Delta t_{n+1} + \Delta t_n$, can be rewritten for $\partial \boldsymbol{U}_{n+1}/\partial t$ as

$$\frac{\partial \boldsymbol{U}_{n+1}}{\partial t} = \frac{\boldsymbol{U}_{n+1}}{\Delta t_{n+1}} - \frac{\boldsymbol{U}_n}{\Delta t_{n+1}} + \frac{\partial^2 \boldsymbol{U}_{n+1}}{\partial t}\frac{\Delta t_{n+1}}{2} - \mathcal{O}(\Delta t_{n+1}^2) \tag{18}$$

$$\frac{\partial \boldsymbol{U}_{n+1}}{\partial t} = \frac{\boldsymbol{U}_{n+1}}{\Delta t_{n+1} + \Delta t_n} - \frac{\boldsymbol{U}_{n-1}}{\Delta t_{n+1} + \Delta t_n} + \frac{\partial^2 \boldsymbol{U}_{n+1}}{\partial t^2}\frac{(\Delta t_{n+1} + \Delta t_n)}{2} - \mathcal{O}((\Delta t_{n+1} + \Delta t_n)^2) \tag{19}$$

The familiar backward Euler time discretization follows directly from Eq. (18) by recognizing

$$\frac{\partial \boldsymbol{U}_{n+1}}{\partial t} = \frac{\boldsymbol{U}_{n+1} - \boldsymbol{U}_n}{\Delta t_{n+1}} + \mathcal{O}(\Delta t_{n+1}) \tag{20}$$

which provides a first-order-in-time approximation upon neglecting the $\mathcal{O}(\Delta t_{n+1})$ term. As such, this scheme yields a fully implicit problem for U_{n+1} that may be used when time accuracy is not required. Alternatively, a linear combination of Eqs. (18) and (19) can be used to annihilate the leading $\partial^2 \boldsymbol{U}_{n+1}/\partial t^2$ term and create a backward second-order-accurate approximation to $\partial \boldsymbol{U}_{n+1}/\partial t$. This approximation, along with Eq. (20), can be generalized in the form

$$\frac{\partial \boldsymbol{U}_{n+1}}{\partial t} = \alpha_t \boldsymbol{U}_{n+1} + \beta_t \boldsymbol{U}_n + \gamma_t \boldsymbol{U}_{n-1} + \mathcal{O}(\Delta t_{n+1}^p) \tag{21}$$

to yield either a first- or second-order-accurate time discretization. The weights α_t, β_t, and γ_t are given for $p = 1$ and 2 in Table 1. Since this second-order scheme requires *two* levels of solution history, it is not self-starting. In practice, five backward Euler steps are taken to develop the required solution history and to allow rapid transients to subside before applying the second-order scheme.

After time discretization using either Eq. (20) or Eq. (21), Eq. (15) can be written in residual form for the unknown nodal values $\boldsymbol{U}_{n+1} \equiv \boldsymbol{U}_h(t_{n+1})$ as the nonlinear algebraic system:

$$\boldsymbol{R}(\boldsymbol{U}_{n+1}) = 0 \tag{22}$$

The goal is then to define a sequence of linear problems that, when solved, converge to obtain the solution $\boldsymbol{U}_{n+1}$ of the nonlinear system (22). Expanding Eq. (22) with a Taylor series about iterate $\boldsymbol{U}_{n+1}^l$ gives

$$\boldsymbol{R}(\boldsymbol{U}_{n+1}^{l+1}) = \boldsymbol{R}(\boldsymbol{U}_{n+1}^l) + \left[\frac{\partial \boldsymbol{R}(\boldsymbol{U}_{n+1}^l)}{\partial \boldsymbol{U}_{n+1}}\right]\delta \boldsymbol{U}_{n+1}^{l+1} + \mathcal{O}((\delta \boldsymbol{U}_{n+1}^{l+1})^2) \tag{23}$$

where $\partial \boldsymbol{R}/\partial \boldsymbol{U}$ is the Jacobian matrix for the nonlinear system and $\delta \boldsymbol{U}_{n+1}^{l+1} = \boldsymbol{U}_{n+1}^{l+1} - \boldsymbol{U}_{n+1}^l$. Truncating this expansion and setting $R(\boldsymbol{U}_{n+1}^{l+1}) = 0$ yields Newton's method:

$$\left[\frac{\partial \boldsymbol{R}(\boldsymbol{U}_{n+1}^l)}{\partial \boldsymbol{U}_{n+1}}\right]\partial \boldsymbol{U}_{n+1}^{l+1} = -\boldsymbol{R}(\boldsymbol{U}_{n+1}^l) \tag{24}$$

which results in an implicit linear system for $\delta \boldsymbol{U}_{n+1}^{l+1}$ and a sequence of iterates $(l = 0, 1, \ldots)$ that converges to $\boldsymbol{U}_{n+1}$. It is important to recall than Newton's method exhibits second-order *conditional* convergence. That is, the magnitude of $R(\boldsymbol{U}_{n+1}^{l+1})$ decreases quadratically at successive iterates provided that the initial guess $\boldsymbol{U}_{n+1}^0$ is sufficiently close to the unknown $\boldsymbol{U}_{n+1}$ [38,39].

Table 1 First- and second-order-accurate time-discretization coefficients

p	α_t	β_t	γ_t
1	$\frac{1}{\Delta t_{n+1}}$	$\frac{-1}{\Delta t_{n+1}}$	0
2	$-\beta_t - \gamma_t$	$-[\frac{1}{\Delta t_{n+1}} + \frac{1}{\Delta t_n}]$	$\frac{\Delta t_{n+1}}{\Delta t_n(\Delta t_{n+1} + \Delta t_n)}$

While the full-Newton scheme is conceptually simple, the implementation is complicated by the nonlinear dependence of the transport properties on the unknowns [see Eq. (4)] and the highly nonlinear nature of the convective terms themselves. In practice, implementing the full-Newton scheme is computationally intensive and, in the case of supersonic flows exhibiting shock waves, is often only of modest benefit. That is, due to the conditional convergence restriction of the method and the sharp gradients or discontinuities that are present in the flowfield, the asymptotic quadratic convergence rate may not be achieved [40]. The implementation of an approximate Newton–Krylov technique to address these issues warrants further discussion.

The Newton scheme results in a series of sparse linear problems of the form

$$\boldsymbol{K}\,\delta \boldsymbol{U}_{n+1} = f \tag{25}$$

which must be solved to obtain $\boldsymbol{U}_{n+1}$. For the discretization presented in Sec. IV using standard piecewise-linear elements, $\boldsymbol{K}$ is a sparse, nonsymmetric, nonsingular matrix. Given the size and sparseness of $\boldsymbol{K}$ it is natural to use preconditioned Krylov subspace iterative techniques to approximate $\delta \boldsymbol{U}_{n+1}$ [41,42]. The essential kernel of these techniques is the computation of the matrix-vector product $\boldsymbol{y} = \boldsymbol{K}\boldsymbol{x}$. Two techniques for providing this kernel will be discussed; the first stores the sparse matrix and computes the matrix-vector product explicitly, and the second computes the action of the matrix-vector product in a matrix-free sense.

One straightforward technique for solving Eq. (25) is to build the system matrix $\boldsymbol{K}$ and right-hand side vector $\boldsymbol{f}$. Since the matrix is large yet sparse, care must be taken to store it efficiently. In the present work, the parallel sparse matrix format implemented in the PETSc toolkit is used, as are the PETSc iterative solvers [37]. When the system matrix is constructed explicitly, it may then be copied and modified to serve as a preconditioner as well. In the current work, a standard parallel block-Jacobi ILU-0 preconditioner is used [41,42]. Once the system matrix and preconditioner are formed, the required matrix-vector products are computed directly.

Recall from Eq. (24) the particular form of the implicit system to be solved:

$$\left[\frac{\partial \boldsymbol{R}}{\partial \boldsymbol{U}}\right]\delta \boldsymbol{U} = -\boldsymbol{R}(\boldsymbol{U})$$

For this special case, the action of the matrix-vector product $[\partial \boldsymbol{R}/\partial \boldsymbol{U}]\delta \boldsymbol{U}$ is nothing more than the derivative of $\boldsymbol{R}$ in the direction specified by $\delta \boldsymbol{U}$ and may be approximated within $\mathcal{O}(\varepsilon)$ for finite ε as

$$\left[\frac{\partial \boldsymbol{R}}{\partial \boldsymbol{U}}\right]\delta \boldsymbol{U} \approx \frac{\boldsymbol{R}(\boldsymbol{U} + \varepsilon \delta \boldsymbol{U}) - \boldsymbol{R}(\boldsymbol{U})}{\varepsilon} \tag{26}$$

From Eq. (26) it is clear that the required matrix-vector product may be approximated by differencing successive residual evaluations. It is in this sense that the scheme is matrix-free: the actual system matrix need not be explicitly formed. All that is required is the capability to evaluate the discrete residual $\boldsymbol{R}(\boldsymbol{U})$. Of course, for practical applications, some form of preconditioning must be applied to the linear system. Depending on the implementation of this preconditioning, the composite scheme may store some approximation of the system matrix. For this reason, some researchers refer to this approach as Jacobian-free [43], since some approximate matrix is usually assembled for preconditioning purposes. Still, one attractive feature of this approach is that it can require substantially less memory than the sparse matrix approach.

Perhaps the most compelling reason to use the matrix-free approach is that it directly yields a quasi-Newton formulation. That is, the finite difference approximation properly accounts for *all* the nonlinearities in the system. This is especially attractive from an algorithm development perspective. For example, alternate shock-capturing terms, SUPG weighting functions, equations of state, and transport property definitions can all be implemented simply by defining their contribution to the discrete residual. Their contribution to the quasi-Newton iteration simply falls out through the approximate matrix-vector product (26). (For a comprehensive review of matrix-free approaches, see the work of Knoll and Keyes [43].)

All computations shown later employ the PETSc toolkit from Argonne National Laboratory [37] to solve the parallel implicit linear systems using the generalized minimum residual Krylov subspace technique [44] with preconditioning. The preconditioner is of parallel block-Jacobi-type, where each processor subblock uses an overlapping additive Schwartz method with an incomplete lower-upper factorization at the subblock level with no fill (ILU-0). Spatial integration is performed with Gauss quadrature rules that are sufficient to integrate third-order polynomials exactly.

VI. Experimental Validation

Two applications are investigated to test the applicability of the model and to assess the behavior and performance of the finite element scheme and solution algorithms described in the previous sections. Experimental data are available for both benchmark problems, and axisymmetry may be exploited to obtain very-high-resolution simulations with mesh-converged approximate solutions. Detailed comparisons of heat transfer and pressure coefficients in regions of interest may thereby be achieved and interpreted.

A. Axisymmetric Hollow-Cylinder Flare

The first configuration examined is an axisymmetric hollow cylinder with a flare inclined at 30°. (The use of axisymmetric models removes the question of width and edge effects that are an issue for two-dimensional configurations and are particularly problematic for shock-interaction problems.) The resulting shock/shock and shock/boundary-layer interactions produce a large localized peak in heat transfer on the model surface. Experimental data were obtained for this configuration at the Calspan—University of Buffalo Research Center (CUBRC) Large Energy National Shock (LENS) tunnel facility [4,5]. A schematic depicting the dimensions and instrumentation layout is shown in Fig. 2. The freestream Mach number is 10.3 and static temperature is 120.4 K. The Reynolds number based on cylinder length is 25,347. The model surface is assumed to be isothermal with no slip, and its temperature is fixed at 295.2 K.

The model was instrumented with a series of thin-film heat transfer gauges and piezoelectric pressure transducers. The reported accuracy of the heat transfer measurements is ±5%. The model was tested in pure nitrogen to minimize chemical nonequilibrium effects in the flow, which would be appreciable in air at the elevated freestream enthalpies used in the test [5]. Previous numerical studies by Gnoffo [7] and MacLean and Holden [6] (all of whom assessed the influence of thermal nonequilibrium) have indicated that the assumption of a calorically perfect gas is valid for this case. The collected data are extremely valuable for validation because the flow conditions are such that complex laminar flow results with minimal chemistry effects.

The computational mesh used for this case is shown in Fig. 1a. It uses a collection of quadrilaterals to encompass the external flow and a portion of the interior just below the sharp leading edge. Including the interior portion of the domain allows the inflow boundary condition to be well-posed. The outer boundary of the grid was tailored such that the wall-normal spacing in the reattachment area is minimized, thus allowing for focused resolution in this high-gradient region. The height of the outflow boundary was chosen such that the oblique shocks produced by the cylinder-displacement thickness and flare would be fully contained within the flow domain. The left and upper boundaries are specified as freestream with essential boundary conditions, and the cylinder flare is modeled as an isothermal no-slip wall. Three nested meshes were used in this simulation. The coarsest mesh contains 45,420 bilinear quadrilateral elements with 46,113 nodes, yielding a discrete problem with 184,452 degrees of freedom. The medium and fine meshes contain 181,680 and 726,720 elements, respectively. The simulation begins with the domain initialized to freestream conditions everywhere, and an initial time step $\Delta t_0 = 10^{-6}$ is used to advance the solution. The time step then grows geometrically with the relative change in the unsteady residual measured over k time steps. Explicitly,

$$\Delta t_{n+1} = \min\left(\Delta t_{n-k} \max\left(\left[\frac{\mathcal{R}_{n-k}}{\mathcal{R}_n}\right]^r, 1\right), \Delta t_{\max}\right) \tag{27}$$

where

$$\mathcal{R}_n \equiv \| \frac{\Delta \boldsymbol{U}_n}{\Delta t} \|_\infty$$

and $r = 1.2$ is the growth rate. The time-step size is updated every $k = 5$ time steps.

Several important flow features are evident from the static temperature field shown in Fig. 3. A weak shock develops at the leading edge of the hollow cylinder due to boundary-layer displacement effects. The flow separates at x/L of approximately 0.55 and creates a separation shock that coalesces with the leading-edge shock. The separation/leading-edge merged shock is then seen to impinge on the conical section in the reattachment region. The strong temperature gradient in the reattachment region at x/L of 1.4 is clearly evident. The peak temperature in the reattachment region is 1450 K (approximately 12 times the freestream value). Clearly, these elevated temperatures would cause significant vibrational excitation of O_2 in air; however, these effects are mitigated by using N_2 as the test gas.

Figure 4 shows a comparison between measured and computed heat transfer and pressure coefficients. The geometry is superimposed on the figure with a faint gray line for reference. Both the trends and magnitudes of the experimental data are well captured by the numerical solution. Separation is clearly evident at x/L of 0.55, as indicated by the increase in pressure coefficient and corresponding decrease in surface heat transfer. The extreme wall-normal temperature gradients in the reattachment region is reflected in increased heat transfer to the surface. The measured peak heat transfer exceeds the computed value, and there is some discrepancy in the heat transfer downstream of the reattachment point. However, similar behavior was seen by MacLean and Holden [6] with two completely different flow solvers, lending some credibility to the current numerical results. During the transient startup phase, before achieving steady state, the forward extent of the separation region increases while the location of the reattachment moves downstream. The peak heating in the reattachment region decreases as the extent of the separated region approaches steady state. (Note that the experimental data are inconsistent in the separation location in that the pressure rise occurs before the heat transfer reduction. This is in contrast to the double-cone data considered later. This may indicate some asymmetry in the test condition, since the heat transfer and pressure measurements are made at different angular positions.)

The iterative convergence is examined in Fig. 5. The figure shows the magnitude of the time derivative, time-step size, and the physical time as a function of time step. It is interesting that the fully implicit finite element discretization, initialized to freestream values, converges to a steady state in approximately 180 time steps. This result is especially promising given that the solution is time-accurate and does not resort to an inconsistent time discretization in order to accelerate convergence, as in the case of so-called local time-stepping methods. The time-step size is also shown in the figure and is allowed to increase geometrically with decreasing residual in accordance with Eq. (27), with the maximum time step limited to $\Delta t_{\max} = 1$. This maximum nondimensional time step is quite aggressive and corresponds to the amount of time required for a point in the freestream to traverse the length of the forward cylinder: that is, $t_{\mathrm{nondim}} = L_{\mathrm{ref}}/U_\infty = 44\ \mu\mathrm{s}$.

The nondimensional simulation time is also shown in Fig. 5, and indicates that steady state is reached in approximately 80 characteristic times. The unsteady residual stagnates at a factor of 10^{-8} below its initial value. The exact reason for this convergence stagnation deserves further investigation but may be related to the shock-

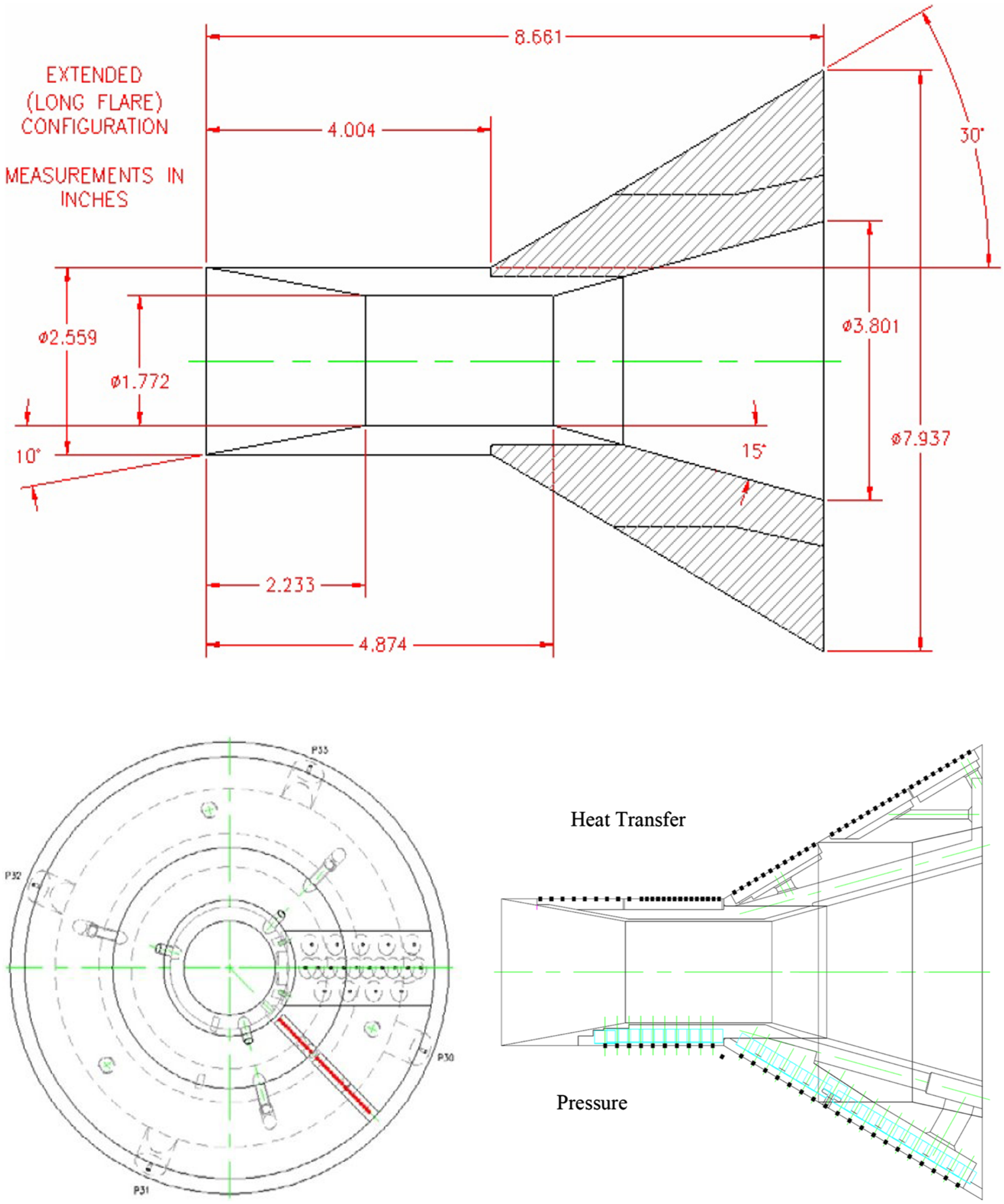

Fig. 2 Hollow-cylinder test article [6].

capturing term. This behavior would be similar to the familiar limiter ringing occasionally observed in the finite volume setting [45]. This behavior will be investigated in depth in future work.

Mesh convergence was investigated using a series of three nested meshes. The surface heat transfer is compared for these three meshes in Fig. 6. The separation point moves upstream to the experimentally observed location as the mesh is refined. The coarsest mesh is obviously inadequate to accurately capture this flowfield. For this coarse mesh, separation is delayed, which is consistent with the behavior expected for a laminar separated flow at lower Reynolds numbers. Thus, in some sense, the additional numerical diffusion introduced by the coarse grid causes the discrete solution to behave as if the flow were at lower Reynolds numbers. The medium and fine meshes correspond to factors of 4 and 16 more elements than the coarse mesh, respectively. These two simulations are found to be in excellent agreement with each other and the majority of the experimental data. The observed discrepancies with experiment are near the reattachment point and slightly downstream, as discussed earlier in this section.

B. Double Cone

Another experimental case with extensive data is that of a geometrically axisymmetric biconic, or double-cone, model. The double cone has been extensively studied and computationally modeled because of the complex shock-interaction structure that results from the compound geometric angle. Experimental data were obtained for a 25°/55° double-cone model at the CUBRC LENS facility [4,5]. Code validation data for four separate nose configurations are available. Here, both the sharp and blunt nose tips with radii of 6.35 mm (0.25 in.) were selected to provide validation data for the finite element scheme. The model geometry and instrumentation layouts are shown in Fig. 7. In the case of the blunt cone, the freestream Mach number is 12.43 and static temperature is 107 K. The Reynolds number based on model base diameter is 53,666. The model wall temperature is assumed to be fixed at 297 K. For the sharp cone, the freestream Mach number is 12.49 and static temperature is 102.2 K. The Reynolds number is 59,259 and the wall temperature is fixed at 295.8 K. It has previously been shown that the test data are

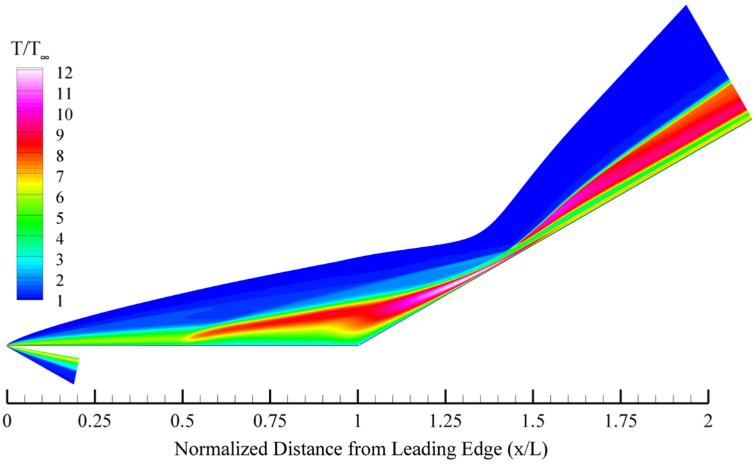

Fig. 3 Illustration of flowfield for hypersonic hollow-cylinder-flare/shock-interaction problem: nondimensional static temperature.

marginally influenced by the effect of vibrational nonequilibrium for these cases [5,6,8].

Previous research has shown that this simple geometry can yield a very complex and potentially unsteady flowfield response [8,46]. Experimental testing was performed in a nitrogen stream at CUBRC for a range of freestream Reynolds numbers [4,5]. Subsequent analysis by Nompelis et al. [8] showed that certain aspects of the experimental results could be best explained by accounting for vibrational nonequilibrium in the freestream. This observation was a result of detailed analysis that accounted for the nonequilibrium expansion within the nozzle to arrive at the freestream conditions that were then fixed as inflow conditions for analysis of the double cone. This previous analysis showed that it is critically important to account for vibrational nonequilibrium when simulating the nozzle expansion process to arrive at the freestream conditions in the test section. These observations are in agreement with previous experimental and computational investigations of double-cone flow performed by Olejniczak [47] that highlighted the sensitivity of these flows to chemical nonequilibrium effects. For the purposes of simulating the double cone at these freestream conditions, however, the calorically perfect assumption is valid [6,8].

The resulting steady-state flowfield for the blunt-nose-tip case is depicted in Fig. 8. Figure 8b shows a computed schlieren image (a grayscale map of density gradient magnitude) for the aforementioned case and depicts details of the complex shock-interaction structure. The image was generated by plotting the magnitude of the density gradient with a grayscale map. As in schlieren photography, strong shock waves create a relatively larger density gradient and appear darker in the image. This is particularly the case in the interaction region, where a nearly normal is shock set up by the 55° cone. (This aft cone angle is beyond the maximum for which an attached oblique shock is possible.) The strength of this shock decreases away from the interaction region as it becomes increasingly oblique. The oblique shock set up by the recirculation region is clearly evident in the figure. This shock overtakes the weak attached shock produced

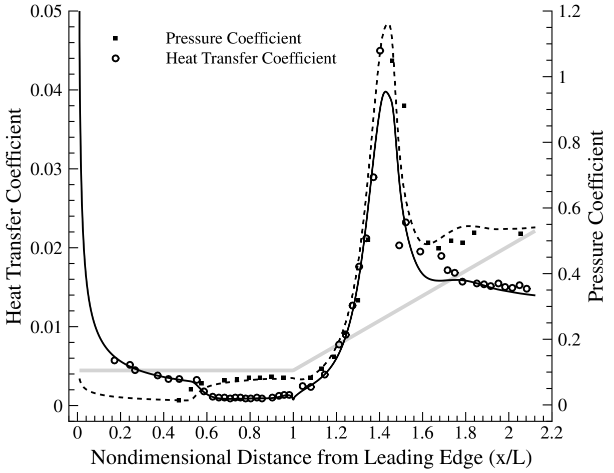

Fig. 4 Comparison of measured and computed heat transfer and pressure coefficients for hollow-cylinder-flare configuration [5,6]. The geometry is superimposed with the faint gray line.

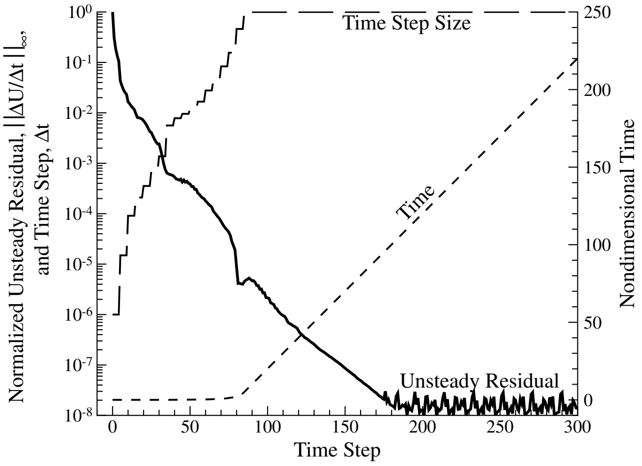

Fig. 5 Iterative convergence for hollow-cylinder-flare configuration.

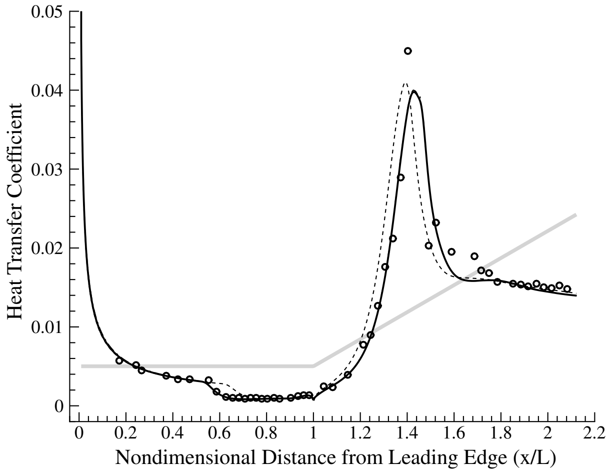

Fig. 6 Surface heat transfer [5,6] for a series of three nested meshes discretizing the hollow-cylinder-flare configuration. The geometry is superimposed with the faint gray line. The results from two finest meshes overlap and are essentially indistinguishable.

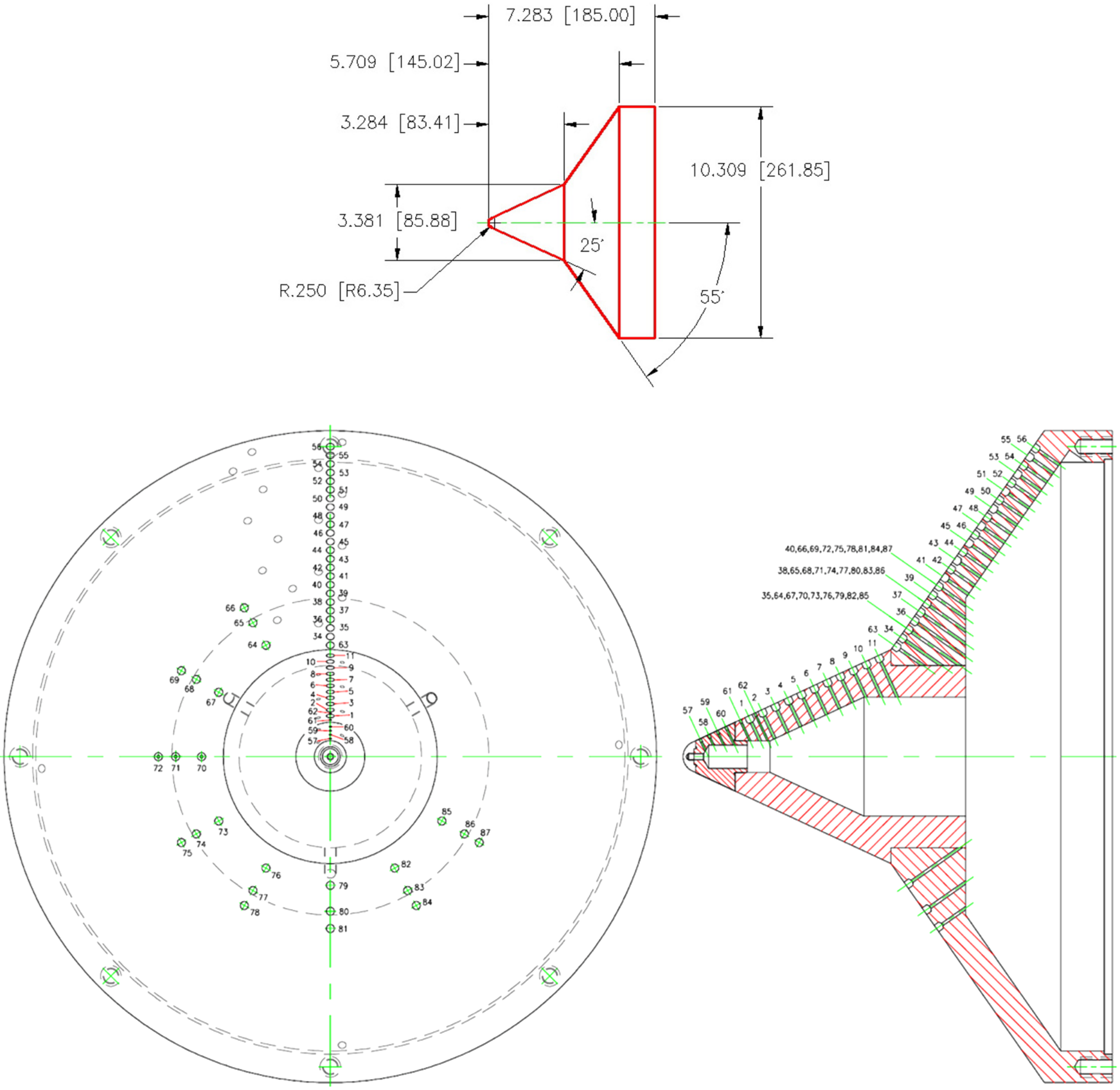

Fig. 7 Double-cone test article [6].

by the 25° forebody and interacts with the detached shock set up by the 55° afterbody. The shock interaction creates a transmitted shock that impacts the model surface, causing a local peak in surface pressure and heat transfer.

The image clearly illustrates the viscous slip surface emanating from the interaction region. This forms a shear layer that separates two distinct regions of flow. Above this feature, the flow is subsonic; below this feature, it is supersonic. This layer forms the boundary for the complex wave reflection pattern that is observed downstream of the interaction. The transmitted shock reflects from the solid surface as a shock, which is then reflected from the shear layer as an expansion. This pattern continues for several cycles downstream: waves reflecting from solid surfaces as the same type and from the slip surface as the opposite type. The numerical results suggest that the shear layer is stable at these moderate Reynolds numbers, but experimental confirmation of this result would be valuable: potentially using planar laser-induced fluorescence seeding or a similar nonintrusive flowfield diagnostic technique [48]. This is of

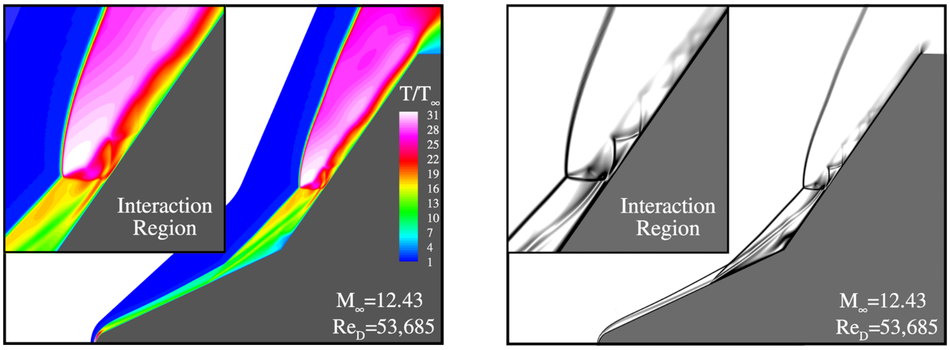

a) Nondimensional static temperature b) Computed schlieren

Fig. 8 Illustration of flowfield for hypersonic blunt-double-cone/shock interaction.

interest because the shear layer has been shown to be a potential source of unsteadiness at higher Reynolds numbers, even for laminar conditions [11,46].

Figure 9 compares the measured and computed surface pressure and heat transfer for this case. Immediately obvious is the large peak in surface pressure and heat transfer caused by the transmitted shock reflecting from the model surface at $(x/L) \approx 1.25$. Additionally, multiple secondary peaks in surface properties are visible on the afterbody region due to the complex wave reflection discussed previously. It is interesting that the heat transfer and pressure on the fore cone upstream of the separation point are not constant (as would be expected for a sharp cone). The variations in these properties are due to the phenomenon of entropy swallowing, which occurs when separate streamlines ingested by the boundary layer contain different entropies. The presence of the blunt nose tip and corresponding curved shock structure induces this behavior. Iterative and mesh convergence studies were performed in a similar fashion to the hollow-cylinder-flare case, but will be omitted for brevity.

Separation is seen to occur on the fore cone at $(x/L) \approx 0.65$, and both experiment and simulation are in excellent agreement about the separation-onset location. This is evident from Fig. 9 by the decrease in heat transfer and associated increase in surface pressure. The magnitude of the heat transfer and surface pressure are in general agreement throughout the entire fore cone $[(x/L) \leq 1]$ in both the attached and separated portions of the flow. The predicted heat transfer on the attached fore cone is slightly higher than the measurements, which is consistent with results from other researchers [6,7]. The experimental values are seen to increase more rapidly than the predicted values on the aft cone, although the trends in both the experimental and computational results are in good agreement. After the peak interaction region, the experiment and computation are again in good agreement, although the highly localized peaks and valleys shown in the computational results seem slightly offset from the experimental measurements.

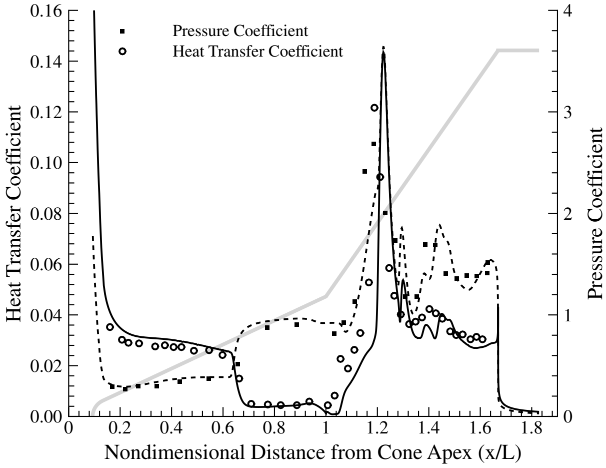

Fig. 9 Comparison of measured and computed heat transfer and pressure coefficients for blunt-cone/cone/shock interaction [5,6]. The geometry is superimposed with the faint gray line.

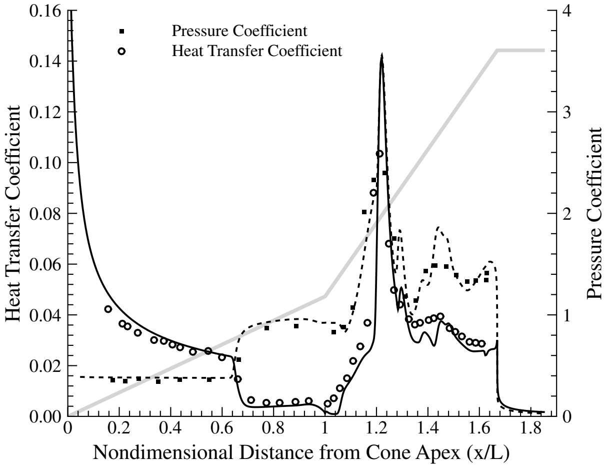

Fig. 10 Comparison of measured and computed heat transfer and pressure coefficients for sharp-cone/cone/shock interaction [5,6]. The geometry is superimposed with the faint gray line.

Figure 10 compares the measured and computed surface pressure and heat transfer for the case of the sharp double cone. (The static temperature and computed schlieren imagery are very similar to those shown for the blunt cone and will be omitted for brevity.) In contrast to the blunt cone, there is no noticeable effect of entropy swallowing in this case. This is clear from the essentially constant pressure on the fore cone. The comparison of experiment and prediction is very similar to the previous case. The pressure and heat transfer are both in good agreement on the fore cone, although the heat transfer predicted from simulation is slightly higher than measured in experiment.

VII. Conclusions

Verification and validation of predicted simulation for compressible atmospheric flow and reentry applications encompass a broad range of experimental endeavors, from fundamental flow physics experiments in laboratories to flight-test data, and a corresponding hierarchy of numerical experiments with studies to scrutinize applicable mathematical models, test numerical methods, and algorithms in the verification process and perform comparison studies with experimental measurements as part of the validation component. The present work focuses on comparison studies with wind-tunnel experiments for the hollow-cylinder-flare and double-cone configurations [4,5] as a central part of the overall validation exercise. The mathematical model for the predictive simulation assumes a laminar calorically perfect gas, which has been shown by previous researchers to be valid for this flow regime [6,7]. The comparison with a viable predictive capability enables both model assessment and testing of the numerical method. The latter point is also important in the present work, since a new numerical approach involving a fully implicit stabilized finite element scheme with grouped-variable treatment of the inviscid flux terms is applied here for the first time to these benchmark problems.

More specifically, the equations form a tightly coupled system of nonlinear partial differential equations that form a mixed parabolic–hyperbolic set for the case of supersonic flows. The stabilized weak form uses the streamline-upwind Petrov–Galerkin (SUPG) finite element method to simulate high-Reynolds-number flows. It is augmented by a modified shock-capturing operator that is required to eliminate spurious oscillations in the vicinity of shock waves. The numerical scheme also uses a grouped-variable approach for discretizing the inviscid flux terms that appear in the stabilized formulation. This approach has proved more stable than the traditional method and has enabled the SUPG finite element scheme to be applied in this work to very complex flows.

The main study compares the available experimentally measured surface pressure and heat transfer distributions for hollow-cylinder-flare and double-cone configurations. In both cases, the data are in good agreement with the model and method (cf. Figs. 4, 9, and 10). Mesh and iterative convergence were demonstrated for the case of the hollow-cylinder flare, as presented in Figs. 5 and 6. The stability afforded by the fully implicit formulation allows for extremely large time steps, resulting in rapid convergence to steady state.

While the model and numerical method are found to be in general agreement with the data in both trends and magnitude, there is some discrepancy in the experimentally measured separation location in the case of the hollow-cylinder flare that could be attributed to flow conditions. For the double cone, the predicted and measured separation locations are in excellent agreement. Additional features such as entropy swallowing in the case of the blunt cone are also reproduced well by the method.

The interpretation of the validation results leads to several observations regarding the efficacy of the numerical method, the suitability of the physical model, and recommendations for further experimental and simulation studies. In particular, future simulations need to assess three-dimensional effects and the influence of freestream uncertainty on predicted results using forward-uncertainty-propagation techniques. This work will be much more computationally intensive and would hence benefit from even more efficient simulation techniques. To this end, adaptive mesh refinement and accelerated sampling approaches are being pursued. Since the implementation is built on the parallel adaptive finite element library libMesh, parallel adaptive simulations are feasible and exploratory investigations of this form are ongoing.

References

[1] *AIAA Guide for the Verification and Validation of Computational Fluid Dynamics Simulations*, Guide G-077-199, AIAA, Reston, VA, 1998.

[2] Babuška, I., Nobile, F., and Tempone, R., "Reliability of Computational Science," *Numerical Methods for Partial Differential Equations*, Vol. 23, No. 4, 2007, pp. 753–784.
doi:10.1002/num.20263

[3] Babuška, I., and Oden, J. T., "Verification and Validation in Computational Engineering and Science: Basic Concepts," *Computer Methods in Applied Mechanics and Engineering*, Vol. 193, Nos. 36–38, Sept. 2004, pp. 4057–4066.
doi:10.1016/j.cma.2004.03.002

[4] Holden, M. S., and Wadhams, T. P., "Database of Aerothermal Measurements in Hypersonic Flow 'Building Block' Experiments," 41st AIAA Aerospace sciences Meeting and Exhibit, AIAA Paper 2003-1137, 2003.

[5] Wadhams, T. P., and Holden, M. S., "Summary of Experimental Studies for Code Validation in the LENS Facility and Comparisons with Recent Navier–Stokes and DSMC Solutions for Two- and Three-Dimensional Separated Regions in Hypervelocity Flows," 42nd AIAA Aerospace Sciences Meeting and Exhibit, AIAA Paper 2004-917, 2004.

[6] MacLean, M., and Holden, M., "Validation and Comparison of WIND and DPLR Results for Hypersonic, Laminar Problems," 42nd AIAA Aerospace Sciences Meeting and Exhibit, AIAA Paper 2004-529, 2004.

[7] Gnoffo, P. A., "Validation studies for hypersonic flow prediction," 39th AIAA Aerospace Sciences Meeting and Exhibit, AIAA Paper 2001-1025, 2001.

[8] Nompelis, I., Candler, G. V., and Holden, M. S., "Effect of Vibrational Nonequilibrium on Hypersonic Double-Cone Experiments," *AIAA Journal*, Vol. 41, No. 11, Nov. 2003, pp. 2162–2169.
doi:10.2514/2.6834

[9] Druguet, M.-C., Candler, G. V., and Nompelis, I., "Effect of Numerics on Navier–Stokes Computations of Hypersonic Double-Cone Flows," *AIAA Journal*, Vol. 43, No. 3, March 2005, pp. 616–623.
doi:10.2514/1.6190

[10] Kirk, B. S., Peterson, J. W., Stogner, R. H., and Carey, G. F., "libMesh: A C++ Library for Parallel Adaptive Mesh Refinement/Coarsening Simulations," *Engineering with Computers*, Vol. 22, No. 3, 2006, pp. 237–254.
doi:10.1007/s00366-006-0049-3

[11] Kirk, B. S., "Adaptive Finite Element Simulation of Flow and Transport Applications on Parallel Computers," Ph.D. Thesis, Univ. of Texas at Austin, Austin, TX, May 2007.

[12] Kirk, B. S., and Carey, G. F., "Development and Validation of a SUPG Finite Element Scheme for the Compressible Navier–Stokes Equations using a Modified Inviscid Flux Discretization," *International Journal for Numerical Methods in Fluids*, Vol. 57, No. 3, May 2008, pp. 265–293.
doi:10.1002/fld.1635

[13] Vincenti, and Kruger, *Introduction to Physical Gas Dynamics*, Krieger, Malabar, FL, 1965.

[14] White, F. M., *Viscous Fluid Flow*, 2nd ed., McGraw–Hill, New York, 1991.

[15] Christie, I., Griffiths, D. F., Mitchell, A. R., and Zienkiewicz, O. C., "Finite Element Methods for Second Order Differential Equations with Significant First Derivatives," *International Journal for Numerical Methods in Engineering*, Vol. 10, No. 6, 1976, pp. 1389–1396.
doi:10.1002/nme.1620100617

[16] Carey, G. F., and Oden, J. T., *Finite Elements: VI, Special Problems in Fluid Mechanics*, Prentice–Hall, Englewood Cliffs, NJ, 1986.

[17] Fries, T.-P., and Matthies, H. G., "A Review of Petrov–Galerkin Stabilization Approaches and an Extension to Meshfree Methods," Inst. of Scientific Computing, Technical Univ. Braunschweig, TR 2004-01, Braunschweig, Germany, March 2004.

[18] Kessler, M. P., and Awruch, A. M., "Analysis of Hypersonic Flows Using Finite Elements with Taylor-Galerkin Scheme," *International Journal for Numerical Methods in Fluids*, Vol. 44, No. 12, 2004, pp. 1355–1376.
doi:10.1002/fld.695

[19] Kolesnikov, A., and Baker, A. J., "An Efficient High-Order Taylor Weak Statement Formulation for the Navier–Stokes Equations," *Journal of Computational Physics*, Vol. 173, No. 2, Nov. 2001, pp. 549–574.
doi:10.1006/jcph.2001.6893

[20] Jiang, B., and Carey, G., "A Stable Least-Squares Finite Element Method for Nonlinear Hyperbolic Problems," *International Journal for Numerical Methods in Fluids*, Vol. 8, No. 8, 1988, pp. 933–942.
doi:10.1002/fld.1650080805

[21] Jiang, B., and Carey, G., "Least-Squares Finite Element Methods for Compressible Euler Equations," *International Journal for Numerical Methods in Fluids*, Vol. 10, No. 5, 1990, pp. 557–568.
doi:10.1002/fld.1650100504

[22] Hughes, T. J. R., Franca, L. P., and Hullbert, G. M., "A New Finite Element Formulation for Computational Fluid Dynamics, VIII: The Galerkin/Least-Squares Method Advective-Diffusive Equations," *Computer Methods in Applied Mechanics and Engineering*, Vol. 73, No. 2, 1989, pp. 173–189.
doi:10.1016/0045-7825(89)90111-4

[23] Hughes, T. J. R., and Mallet, M., "A New Finite Element Formulation for Computational Fluid Dynamics, III: The Generalized Streamline Operator for Multidimensional Advective-Diffusive Systems," *Computer Methods in Applied Mechanics and Engineering*, Vol. 58, No. 3, 1986, pp. 305–328.
doi:10.1016/0045-7825(86)90152-0

[24] Shakib, F., Hughes, T. J. R., and Johan, Z., "A New Finite Element Formulation for Computational Fluid Dynamics, X: The Compressible Euler and Navier–stokes Equations," *Computer Methods in Applied Mechanics and Engineering*, Vol. 89, Nos. 1–3, 1991, pp. 141–219.
doi:10.1016/0045-7825(91)90041-4

[25] Aliabadi, S. K., "Parallel Finite Element Computations in Aerospace Applications," Ph.D. Thesis, Univ. of Minnesota, Minneapolis, MN, 1994.

[26] Aliabadi, S. K., and Tezduyar, T. E., "Parallel Fluid Dynamics Computations in Aerospace Applications," *International Journal for Numerical Methods in Fluids*, Vol. 21, No. 10, 1995, pp. 783–805.
doi:10.1002/fld.1650211003

[27] Hughes, T. J. R., Scovazzi, G., and Tezduyar, T. E., "Stabilized Methods for Compressible Flows," Inst. for Computational Engineering and Sciences, Rept. 08-04, Austin, TX, March 2008, http://www.ices.utexas.edu/research/reports/2008/0804.pdf [retrieved 25 March 2010].

[28] LeBeau, G. J., "The Finite Element Computation of Compressible Flows," M.S. Thesis, Univ. of Minnesota, Minneapolis, MN, 1990.

[29] Hughes, T. J. R., and Mallet, M., "A New Finite Element Formulation For Computational Fluid Dynamics, IV: A Discontinuity Operator For Multidimensional Advective-Diffusive Systems," *Computer Methods in Applied Mechanics and Engineering*, Vol. 58, No. 3, 1986, pp. 329–336.
doi:10.1016/0045-7825(86)90153-2

[30] Hauke, G., and Hughes, T. J. R., "A Comparative Study of Different Sets of Variables for Solving Compressible and Incompressible Flows," *Computer Methods in Applied Mechanics and Engineering*, Vol. 153, Nos. 1–2, 1998, pp. 1–44.
doi:10.1016/S0045-7825(97)00043-1

[31] Bonhaus, D. L., "A Higher Order Accurate Finite Element Method for Viscous Compressible Flows," Ph.D. Thesis, Virginia Polytechnic Inst. and State Univ., Blacksburg, VA, Nov. 1998.

[32] Gropp, W. D., Kaushik, D. K., Keyes, D. E., and Smith, B. F., "High Performance Parallel Implicit CFD," *Parallel Computing*, Vol. 27, No. 4, 2001, pp. 337–362.
doi:10.1016/S0167-8191(00)00075-2

[33] Hovland, P. D., and McInnes, L. C., "Parallel Simulation of Compressible Flow Using Automatic Differentiation and PETSc," *Parallel Computing*, Vol. 27, No. 4, 2001, pp. 503–519.
doi:10.1016/S0167-8191(00)00074-0

[34] Tannehill, J. C., Anderson, D. A., and Pletcher, R. H., *Computational Fluid Mechanics and Heat Transfer*, 2nd ed., Taylor & Francis, Washington, D.C., 1997.

[35] Kaushik, D., Keyes, D., and Smith, B., "Newton-Krylov-Schwarz Methods for Aerodynamic Problems: Compressible and Incompressible Flows on Unstructured Grids," *Proceedings of the Eleventh*

International Conference on Domain Decomposition Methods, Domain Decomposition Press, Bergen, Norway, 1999, pp. 513–520.

[36] Karypis, G., and Kumar, V., "METIS Unstructured Graph Partitioning and Sparse Matrix Order," Univ. of Minnesota, Department of Computer Science, Minneapolis, MN,Aug. 1995.

[37] Balay, S., Buschelman, K., Eijkhout, V., Gropp, W. D., Kaushik, D., Knepley, M. G., et al., "PETSc Users Manual," Argonne National Lab., TR ANL-95/11, Rev. 2.3.0, Argonne, IL, April 2004.

[38] Iserles, A., *A First Course in the Numerical Analysis of Differential Equations*, Cambridge Univ. Press, New York, 1996.

[39] Greenberg, M. D., *Foundations of Applied Mathematics*, Prentice–Hall, Upper Saddle River, NJ, 1978.

[40] Johan, Z., Hughes, T. J. R., and Shakib, F., "A Globally Convergent Matrix-Free Algorithm for Implicit Time-Marching Schemes Arising in Finite Element Analysis in Fluids," *Computer Methods in Applied Mechanics and Engineering*, Vol. 87, Nos. 2–3, 1991, pp. 281–304. doi:10.1016/0045-7825(91)90009-U

[41] Barrett, R., Berry, M., Chan, T. F., Demmel, J., Donato, J. M., Dongarra, J., Eijkhout, V., Pozo, R., Romine, C., and der Vorst, H. V., *Templates for the Solution of Linear Systems: Building Blocks for Iterative Methods*, Society for Industrial and Applied Mathematics, Philadelphia, 1994, http://www.netlib.org/templates/Templates.html [retrieved Feb. 2010].

[42] Golub, G. H., and Van Loan, C. F., *Matrix Computations*, 3rd ed., Johns Hopkins Univ. Press, Baltimore, MD, 1996.

[43] Knoll, D. A., and Keyes, D. E., "Jacobian-Free Newton-Krylov Methods: A Survey of Approaches and Applications," *Journal of Computational Physics*, Vol. 193, No. 2, Jan. 2004, pp. 357–397. doi:10.1016/j.jcp.2003.08.010

[44] Saad, Y., and Schultz, M. H., "GMRES: a Generalized Minimal Residual Algorithm for Solving Nonsymmetric Linear Systems," *SIAM Journal on Scientific and Statistical Computing*, Vol. 7, No. 3, 1986, pp. 856–869. doi:10.1137/0907058

[45] Venkatakrishnan, V., "Convergence To Steady State Solutions of the Euler Equations on Unstructured Grids with Limiters," *Journal of Computational Physics*, Vol. 118, No. 1, April 1995, pp. 120–130. doi:10.1006/jcph.1995.1084

[46] Coblish, J. J., Smith, M. S., Hand, T., Candler, G. V., and Nompelis, I., "Double-Cone Experiment and Numerical Analysis at AEDC Hypervelocity Wind Tunnel No. 9," 43rd AIAA Aerospace Sciences Meeting and Exhibit, AIAA Paper 2005-0902, 2005.

[47] Olejniczak, J., *Computational and Experimental Study of Nonequilibrium Chemistry in Hypersonic Flows*, Ph.D. Thesis, Univ. of Minnesota, Minneapolis, MN, April 1997.

[48] Inman, J. A., Danehy, P. M., Alderfer, D. W., Buck, G. M., and McCrea, A., "PLIF Imaging of Capsule RCS Jets, Shear Layers, and Simulated Forebody Ablation," AIAA Paper 2008-0248, Jan. 2008.

X. Zhong
Associate Editor